J. Chem. Thermodynamics 97 (2016) 244–252

Contents lists available at ScienceDirect

J. Chem. Thermodynamics

journal homepage: www.elsevier.com/locate/jct

Melting behaviour of americium-doped uranium dioxide

D. Prieur [a], F. Lebreton [b], M. Caisso [c,d], P.M. Martin [b], A.C. Scheinost [e], T. Delahaye [d], D. Manara [a,*]

[a] European Commission, Joint Research Centre, Institute for Transuranium Elements (JRC-ITU), P.O. Box 2340, 76125 Karlsruhe, Germany
[b] CEA, DEN, DTEC/SECA/LCC, F-30207 Bagnols-sur-Cèze Cedex, France
[c] CEA, DEN, DTEC/SECA/LFC, F-30207 Bagnols-sur-Cèze Cedex, France
[d] CEA, DEN, DRCP/SERA/LCAR, F-30207 Bagnols-sur-Cèze Cedex, France
[e] Helmholtz Zentrum Dresden Rossendorf (HZDR), Institute of Resource Ecology, P.O. Box 10119, 01314 Dresden, Germany

ARTICLE INFO

Article history:
Received 3 November 2015
Received in revised form 27 January 2016
Accepted 3 February 2016
Available online 10 February 2016

Keywords:
Uranium
Americium
Nuclear fuel
High temperature
Melting
XAS

ABSTRACT

(Uranium + americium) mixed oxides are considered as potential targets for americium transmutation in fast neutron reactors. Their thermophysical properties and notably their melting behaviour have not been assessed properly although required in order to evaluate the safety of these compounds under irradiation. In this study, we measured via laser heating, the melting points under inert atmosphere (Ar) of $U_{1-x}Am_xO_{2\pm\delta}$ samples with $x = 0.10, 0.15, 0.20$. The obtained melting/solidification temperatures, measured here, indicate that under the current experimental conditions in the investigated AmO_2 content range, the *solidus* line of the (UO_2 + AmO_2) system follows with very good agreement the ideal solution behaviour. Accordingly, the observed *liquidus* formation temperature decreases from (3130 ± 20) K for pure UO_2 to (3051 ± 28) K for $U_{0.8}Am_{0.2}O_{2\pm\delta}$. The melted and quenched materials have been characterised by combining X-ray diffraction and X-ray absorption spectroscopy.

1. Introduction

Americium is a minor actinide (MA) produced in nuclear fuels during their irradiation in reactors. Despite the low amount generated (about 0.07 wt.% of spent fuel irradiated in standard conditions), Am isotopes account for a significant contribution to the long-term radiotoxicity and heat load of spent fuels [1]. Partitioning and Transmutation (P&T) is a promising strategy to decrease this contribution notably through the heterogeneous transmutation. This mode consists in incorporating Am into UO_2 to form (U + Am) mixed dioxides ($U_{1-x}Am_xO_{2\pm\delta}$). This transmutation fuel, designated as AmBB (americium-bearing blankets) would ultimately be irradiated in the periphery of FNR (fast neutron reactor) cores. The radiotoxicity and heat load of ultimate nuclear waste would thus be decreased as well as the ecological footprint of deep geological repositories [2,3]. In this context, several studies have been dedicated to $U_{1-x}Am_xO_{2\pm\delta}$ compounds, not only to investigate synthesis methods [4–11] and assess their behaviour under irradiation in reactors [4,7,12,13], but also to determine their structural and thermophysical properties, the latter remaining scarcely known [14–20]. Among them, no data regarding the $U_{1-x}Am_xO_{2\pm\delta}$ melting behaviour has been reported, despite the importance of such information with respect to safety margins during irradiation, notably in accidental conditions.

In this study we investigate the melting behaviour under an inert (argon) atmosphere of $U_{1-x}Am_xO_{2\pm\delta}$ compounds with $x = 0.10, 0.15, 0.20$, which corresponds to compositions close to those envisaged for AmBB (the current reference being 10 mol.%-Am). The method used for the melting experiments is based on laser heating and a self-crucible approach in order to avoid sample-crucible interactions during the measurements. It was recently applied to UO_2 [21], PuO_2 [22,23], $U_{1-x}Pu_xO_2$ [24,25] and MA-doped $U_{1-x}Pu_xO_2$ samples [26], and proved to give more accurate values than those previously obtained through more traditional thermal analysis methods [24,25,27]. The samples were also characterised after melting using powder X-ray Diffraction (XRD) and X-ray Absorption Spectroscopy (XAS). A comparison between pre and post-melting structure (local and long-range) and cationic charge distribution can thus be proposed, based on XRD/XAS characterisation of the same compounds already published in the literature [5,17,18,20].

2. Experimental

2.1. Sample synthesis

The samples were synthesized using two different processes. The chemical compositions are presented in table 1. The 10 and

* Corresponding author.
E-mail address: dario.manara@ec.europa.eu (D. Manara).

http://dx.doi.org/10.1016/j.jct.2016.02.003
0021-9614/

TABLE 1
Impurity content (wt.%) measured by inductively coupled plasma mass spectroscopy. The experimental uncertainties are provided in the table. (*precursor for the synthesis of $U_{0.85}Am_{0.15}O_{2\pm\delta}$, **precursor for the synthesis of $U_{0.90}Am_{0.10}O_{2\pm\delta}$ and $U_{0.80}Am_{0.20}O_{2\pm\delta}$.)

	UO_2^*	AmO_2^*	UO_2^{**}	AmO_2^{**}	$U_{0.90}Am_{0.10}O_{2\pm\delta}$	$U_{0.85}Am_{0.15}O_{2\pm\delta}$	$U_{0.80}Am_{0.20}O_{2\pm\delta}$
				Weight per cent impurity			
C	0.07 ± 0.02		0.56 ± 0.05		0.41 ± 0.05	0.05 ± 0.02	0.40 ± 0.05
Na		0.18 ± 0.05	0.06 ± 0.02		0.04 ± 0.02	0.03 ± 0.02	0.06 ± 0.02
Si		0.58 ± 0.05	0.05 ± 0.02		<0.02	0.07 ± 0.02	0.04 ± 0.02
Fe		<0.02	<0.02		<0.02	<0.02	<0.02
Th	0.15 ± 0.02					0.13 ± 0.02	
U		0.17 ± 0.05		0.05			<0.02
Np		2.6 ± 0.5		0.9	0.05 ± 0.02	0.40 ± 0.05	0.30 ± 0.05

TABLE 2
Sample characteristics and measured melting/solidification points. Data were measured at a buffer gas (argon) pressure of 0.30 ± 0.02 MPa.

Sample	Measured Am/(U + Am) ratio (mol.%)	Sintering conditions	Average *solidus* temperature ± 1σ	Number of successful laser melting pulses
$U_{0.90}Am_{0.10}O_{2\pm\delta}$	8.7 ± 0.3	4 h at T = 1923 K under (Ar + H_2) (4 mol.%)	T = (3070 ± 24) K	5
$U_{0.85}Am_{0.15}O_{2\pm\delta}$	14.8 ± 0.3	4 h at T = 2023 K under (Ar + H_2) (4 mol.%)	T = (3071 ± 29) K	9
$U_{0.80}Am_{0.20}O_{2\pm\delta}$	18.9 ± 0.3	4 h at T = 1923 K under (Ar + H_2) (4 mol.%)	T = 3051 ± 28) K	4

20 mol.%-Am samples were synthesized at Joint Research Centre – Institute for Transuranium Elements (JRC-ITU) using a process based on combination of (sol + gel) and infiltration methods to produce non-contaminant beads used as precursors for sintering [5,28]. The 15 mol.%-Am samples were prepared at Commissariat à ÍEnergie Atomique et aux énergies alternatives (CEA) from $UO_{2+\delta}$ and $AmO_{2-\varepsilon}$ starting powders (similar to those described in [7,8]) following the UMACS process based on two successive thermal treatments separated by a grinding step [7]. The sample characteristics are summarized in table 2.

2.2. Laser melting

The melting behaviour of the current mixed (uranium + americium) dioxides was studied by laser heating and fast multi-channel pyrometry, an experimental method developed at JRC-ITU [21–26]. Details of the laser-heating setup used in this research have been reported in previous publications [21–26], although the technique has been partially modified in the present work. During the laser shots, a mixed oxide disk was held in a sealed autoclave under a controlled atmosphere of pressurized argon in which the absolute pressure of oxygen was checked and was lower than 10 Pa. Such controlled atmosphere permitted, together with the relatively short duration of the experiments, to minimise possible sample decomposition, particularly linked to oxidation or oxygen losses, depending on the initial composition. This approach aims to maintain the sample integrity and its composition as close as possible to its initial value throughout the melting/freezing process.

Thermograms were measured by sub-millisecond resolution pyrometry on samples laser heated beyond melting by a TRUMPF® Nd:YAG cw laser (1064.5 nm). Its power vs. time profile is programmable with a resolution of 1 ms. Pulses of different duration (100 ms to 1000 ms) and maximal power (315 W to 585 W) were repeated on a 5 mm diameter spot on a single sample surface as well as on different samples of the same composition in order to obtain datasets of at least four usable melting/solidification temperature values for each composition (see table 1). Given the limited amount and the high radioactivity of the investigated material, this dataset size was considered to be satisfactory, in that it permitted to obtain significant average values and standard deviations for each composition. The laser pulses lead to maximum temperatures between 3350 K and 3550 K. These temperatures compared with the expected values of the solid/liquid phase transitions for the pure dioxides [21–25,27,29], can be considered to be high enough to melt a sufficient amount of material to obtain a consistent thermal analysis during the cooling stage of the experiments.

Excessive thermal shocks were minimised by starting each series of laser pulses from a pre-set temperature of about 1500 K, at which each sample was held, by low-power laser irradiation, for 30 s to 1 min before starting a series of high-power laser shots. The pre-heating treatment yielded also a better homogenization of the sample surface. Each series consisted of three to four (heating + cooling) pulses on the same sample spot without cooling the material below T = 1500 K. This number of pulses was empirically optimised in order to obtain a minimum number of usable data while minimising the risk of sample breaking. In fact, a sample would mostly break while rapidly cooling to room temperature. On the other hand, no more than four pulses were repeated on each cycle in order to be able to check the sample morphology regularly between one cycle and the next one. The peak intensity and duration of the high-power pulses were increased from one (heating + cooling) cycle to the other, in order to check the result repeatability under slightly different experimental conditions. This approach constituted a step forward in the laser heating technique. It ensured a better mechanical stability of the samples, on which several successive shots could be repeated to check the result reproducibility and the eventual effects of non-congruent vapourization or segregation phenomena. The onset of melting was detected by the appearance of vibrations in the signal of a probe laser (Ar + cw 750 mW to 1.5 W) reflected by the sample surface (Reflected Light Signal technique, or RLS).

The sample cooled naturally when the laser beam was switched off during the thermal cycle. Thermal arrests corresponding to exothermic phase transitions were then observed on the thermograms recorded by the fast pyrometers. These operate in the visible-near infrared range between 488 nm and 900 nm. The reference pyrometer wavelength was 655 nm and was calibrated according to a procedure previously reported [21–26]. The normal spectral emissivities (NSE) of actinide dioxides, necessary for the determination of the sample temperature, have already been studied in detail in earlier publications [21–23]. Based on these previous studies and on theoretical models [21–26], the NSE of mixed (uranium + americium) dioxide samples is assumed to be wavelength-independent in the present spectral range (grey-body approximation). Under such hypothesis, the current multi-wavelength pyrometry approach yielded a constant value of NSE = 0.80 ± 0.04, valid for all the investigated compositions within the reported experimental uncertainty on the NSE. This value has

been used to correct the radiance signal recorded by the pyrometers and convert it, through Planck's blackbody law, into real absolute temperature. The error affecting the final real temperature value due to the emissivity uncertainty was calculated to be $T = \pm 21$ K at $T = 3050$ K.

The total uncertainty of the temperature measurements was determined according to the error propagation law, taking into account the standard uncertainty associated to the pyrometer calibration $T = (\pm 10$ K at 3000 K), the sample emissivity $T = (\pm 21$ K at 3050 K) and the accuracy in detecting the onset of vibrations in the RLS signal. The estimated cumulative uncertainty is thus approximately ±1% of the reported temperatures in the worst cases, with a $1 - k$ coverage factor (corresponding to one standard deviation around the average value) [21–26].

2.3. X-ray diffraction

XRD analyses were performed on the laser heated samples with a Bruker D8 X-ray diffractometer mounted in a Bragg–Brentano configuration, with a curved Ge monochromator (1 1 1), a ceramic Cu X-ray tube (40 kV, 40 mA) and a Linx-eye detector. Scans were collected from 20° to 120° in 2θ using 0.0086° step-intervals with counting steps of 5 s. Structural analysis was performed by the Rietveld method using the JANA2006 software [30].

2.4. X-ray absorption spectroscopy

The XAS measurements were performed at the European Synchrotron Radiation Facility (ESRF, Grenoble, France) on the Rossendorf Beamline (BM20) with a current of (170 to 200) mA in the storage ring (at 6.0 GeV) [31].

The XAS spectra were collected on the melted samples at the U L_{III} (17,166 eV), Am L_{III} (18,510 eV) and U L_{II} edges (20,948 eV) in both transmission and fluorescence mode using *Oxford* ionisation chambers and a *Canberra* energy-dispersive 13-element Ge solid-state detector with a digital amplifier (XIA-XMAP). A double Si (1 1 1) crystal monochromator was used for energy selection and the energy calibration was performed using metallic foils for whose K edges are close to the edges of interest, *i.e.* Y (K-edge energy at 17,038 eV), Zr (K-edge energy at 17,998 eV) and Mo (K-edge energy at 20,000 eV). XANES spectra were recorded at the U and Am L_{III} edges, whereas Am L_{III} and U L_{II} were used for EXAFS measurements (up to a wave vector $k = 18$ and 13.5 $Å^{-1}$, respectively). U L_{II} is preferred to U L_{III} because of the presence of neptunium in the samples (produced by α-decay of ^{241}Am).

Data analyses and refinements were performed using the *Athena* and *Artemis* programs [32,33] and *FEFF 8.40* for ab initio calculations of EXAFS spectra. XANES spectra were normalised using a linear function and a 2nd order polynomial for pre- and post-edge approximation, respectively. The first zero crossings of the first and second energy derivatives were used to determine the white line (WL) and inflection point (E_0) energy positions, respectively. Average oxidation states of the cations were determined by Linear Combination Fitting (LCF) of the experimental normalised absorption spectra by using well-known reference spectra. The reference compounds used were $U^{+IV}O_{2.00(1)}$ [34], $(U^{+IV}_{½}U^{+V}_{½})_4O_9$ [34] and $(U^{+V}_{⅔}U^{+VI}_{⅓})_3O_8$ [35] as well as $Am^{+IV}O_2$ [36,37] and an oxalate $((U^{+IV}_{0.9}Am^{+III}_{0.1})_2(C_2O_4)_5{,}6{\cdot}H_2O)$ [35,36]. The XANES spectra of the reference compounds have been recorded previously at the same beamline. The LCF region is [−20; 30 eV] relatively to the WL position. Uncertainty that for the determined molar fractions is 2 mol.% and for O/M ratio is 0.01. Fourier transforms of the EXAFS spectra were extracted using a Hanning window between 3.5 and 11 $Å^{-1}$, and 3.5 and 14 $Å^{-1}$ for U L_{II} and Am L_{III} edges, respectively, in both cases with a Δk-factor of 2.

One structural model has been used for ab initio EXAFS calculations. It corresponds to a standard fluorite structure in which each cation is surrounded by 8 oxygen anions at $a \times (3)^{1/2}/4$, 12 cations at $a \times (2)^{1/2}/2$, 24 oxygen anions at $a \times (11)^{1/2}/4$ and 6 cations at a, with a the lattice parameter. The four corresponding two-legged paths were included to fit the EXAFS spectra. Two three-legged and two four-legged multiple scattering paths were also chosen, based on their relative high magnitudes. Fits were performed between 1.6 and 6 Å at both the U L_{II} and Am L_{III} edges, with a k-weight value of 3. As often employed for An L_{III}/L_{II} [18,38–40], the amplitude factor (S_0^2) was set at 0.90 for U and Am shells. The shift in the threshold energy (ΔE_0) was varied as a global parameter.

3. Results and discussion

3.1. Pre-melting characterisation

Before conducting the laser heating experiment, the materials have been characterised by XRD and XAS, those results have been already published [5,41]. It was shown that the compounds are fluorite solid solutions for all Am contents. Regarding the charge distribution, equimolar proportions of Am^{+III} and U^{+V} have been measured in $U_{0.85}Am_{0.15}O_{2\pm\delta}$ [17,18,20] meaning that the O/M ratio is close to 2.00. On the contrary, only U(IV) has been reported for the $U_{0.90}Am_{0.10}O_{2\pm\delta}$ and $U_{0.80}Am_{0.20}O_{2\pm\delta}$ compounds used in this work, suggesting the hypo-stoichiometry of these materials [5]. Nevertheless, the EXAFS results obtained for the 20% sample clearly shows a shorter (U + O) first distance and a longer (Am + O) compared to values expected from cell parameter. Such results would suggest a Am^{+III} and U^{+V} charge compensation as recently observed for different $U_{0.90}Am_{0.10}O_{2\pm\delta}$ and $U_{0.80}Am_{0.20}O_{2\pm\delta}$ samples. Hence, considering the apparent disagreement between XANES and EXAFS results in Vespa et al. [5] and surface oxidation observed for such samples an O/M close to 2.00 is assumed for all the samples.

3.2. (Melting+freezing) temperatures

The experimental thermograms recorded on mixed $U_{1-x}Am_xO_{2\pm\delta}$ oxides in an inert atmosphere (pressurized argon at 0.30 ± 0.01 MPa) are quite similar for each composition. For this reason and also for the sake of clarity, only one example is provided in figure 1.

Based on previous experience [21–26], pressurized argon was chosen as the best atmosphere to maintain, as much as possible throughout the heating/cooling cycles, the O/M ratio, nominally at 2.00 in the initial fresh samples. For these experiments, no clear evolution of the freezing thermal arrests can be observed over successive shots on the same sample, confirming that the initial composition is maintained throughout the thermal cycles. The average melting/freezing points measured in this work ($T = 3070$ K ± 24 K, $T = 3071$ K ± 29 K and $T = 3051$ ± 28 K, for respective Am/(U + Am) ratios of 10, 15 and 20mol.%) are reported in table 1 and plotted as a function of the Am content in figure 2. Based on previous investigations performed on other material systems [24,25], this melting/freezing points can be assigned to the *solidus* transition at the studied compositions, whereby *solidus* and *liquidus* temperatures are too close together to be effectively distinguishable with the present experimental approach. It can be seen that the addition of Am to UO_2 leads to a lower melting/freezing temperature, whereas no relevant changes on the thermogram shape can be noticed. Such a behaviour is consistent with the *solidus* and *liquidus* temperatures being close enough, at the investigated compositions, not to be distinguishable using the current technique. The solid/liquid transition temperature thus decreases from an average value of (3120 ± 20) K in pure UO_2 to (3051 ± 28) K in $U_{0.80}Am_{0.20}O_{2\pm\delta}$.

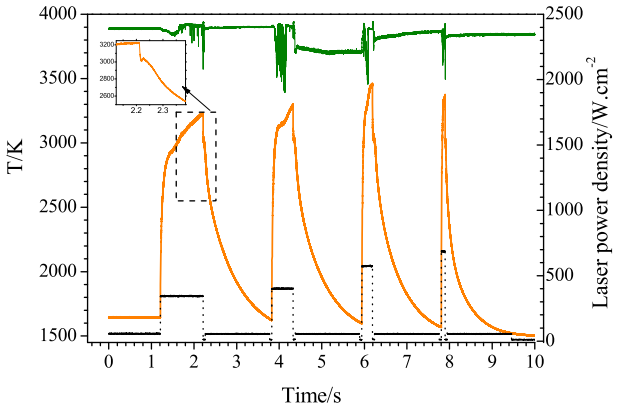

FIGURE 1. Example of experimental thermogram (orange) recorded on a mixed $U_{0.20}Am_{0.80}O_{2\pm\delta}$ oxide in pressurized argon at 0.30 ± 0.01 MPa. The RLS and the laser power are represented in green and black, respectively. (For interpretation of the references to colour in this figure legend, the reader is referred to the web version of this article.)

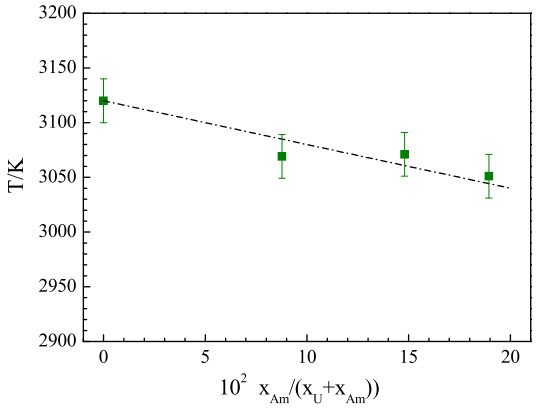

FIGURE 2. Average melting/freezing points in argon as a function of the Am/(U + Am) ratio. The dotted line is an estimation extrapolated from Kato et al. based on measurements and ideal solution calculations up to Am/(U + Am) ratios of 7 mol.%. The melting/freezing temperature of UO_2 was determined in a previous work [21].

3.3. Characterisation of the laser-melted samples

3.3.1. Charge distribution of the laser-melted samples

XANES spectra at both Am L_{III} and U L_{III} edges are compared to those of reference compounds in figure 3. Both inflection point (E_0) and white line (WL) positions are provided in table 3.

At the Am L_{III} edge, the spectra of all three samples are well-aligned with the Am^{+III} reference. A linear combination analysis of the data based on Am^{+IV} and Am^{+III} reference samples indicates a molar fraction of Am^{+III} equal to 100%. Hence, Am remains trivalent in argon as would have been expected [42].

At the U L_{III} edge, an analysis of the inflection point and white line maximum positions suggests that U oxidation states in the samples are comprised between those of $U^{+IV}O_{2.00}$ and $(U^{+IV}_{0.5}U^{+V}_{0.5})_4O_9$ reference compounds, exception made of $U_{0.80}Am_{0.20}O_{2\pm\delta}$, for which the inflection point is close to that of U_4O_9, whereas its white line maximum is at a higher energy. As presented in table 3, the corresponding U^{+IV} and U^{+V} mole fractions were assessed from a linear combination of reference compound spectra.

3.3.2. Structure of the $U_{0.90}Am_{0.10}O_{2\pm\delta}$ and $U_{0.85}Am_{0.15}O_{2\pm\delta}$ laser-melted samples

The XRD patterns of the mixed $U_{1-x}Am_xO_{2\pm\delta}$ oxides are presented in figure 4. After melting, $U_{0.90}Am_{0.10}O_{2\pm\delta}$ and $U_{0.85}Am_{0.15}O_{2\pm\delta}$ remain single fluorite-type phases whose lattice parameters are summarized in table 4. According to the O/M ratio derived from the XANES, the $U_{0.90}Am_{0.10}O_{2\pm\delta}$ solid solution melted in argon is slightly hyper-stoichiometric while the $U_{0.85}Am_{0.15}O_{2\pm\delta}$ oxide remains stoichiometric as the as-synthesized material [41].

The experimental and fitted EXAFS k^3-spectra at Am L_{III} and U L_{II} edges and corresponding Fourier transforms are provided in figures 5 and 6, respectively. An immediate inspection of the Am L_{III} and U L_{II} data shows that there are no significant differences in the periodicity of the oscillations, suggesting similar local structures for $U_{0.90}Am_{0.10}O_{2\pm\delta}$ and $U_{0.85}Am_{0.15}O_{2\pm\delta}$. A good agreement between the experimental and fitted data is observed also, confirming the validity of the structural model used in the present analysis. The crystallographic parameters derived from EXAFS spectra fitting are reported in table 5. The first (Am + O) distance, equal to $(2.42 \pm 0.01)10^{-1}$ nm, is in agreement with that expected for a pure (Am^{+III} + O) distance [43] ($r(Am^{+III})$ = 0.109 nm, $r(Am^{+IV})$ = 0.095 nm, $r(O^{-II})$ = 0.140 nm [44]). The first (U + O) distance $(2.33 \pm 0.01)10^{-1}$ nm is slightly shorter than in $U^{IV}O_{2.00}$ $(2.37 \pm 0.01)10^{-1}$ nm, which is consistent with the $U^{+IV/V}$ mixed valence considering U^{+IV} and U^{+V} ionic radii, ($r(U^{+IV})$ = 0.100 nm, $r(U^{+V})$ = 0.089 nm [44]). The (Me + Me) bond lengths are about $(3.86 \pm 0.01)10^{-1}$ nm for both Am and U, indicating a random distribution in the cationic sub-lattice. One can then observe that Am and U local environments are similar to those previously reported [17,18,45–47]. At the U L_{II} edge, the Debye–Waller factors are slightly larger to those of the as-synthesized materials [17,18,20], which suggests a higher structural disorder and agrees with the slight hyper-stoichiometry. On the contrary, no variation of the

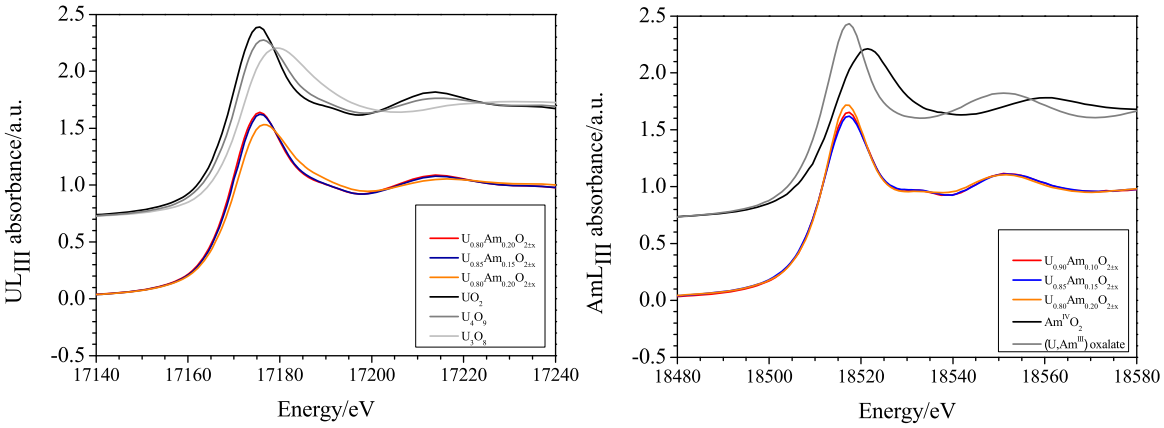

FIGURE 3. XANES spectra of the laser-melted samples at the U L_{III} edge (left) and Am L_{III} edge (right).

TABLE 3
White line (WL) and inflection point (E_0) positions for laser-melted $U_{1-x}Am_xO_{2\pm\delta}$ samples and reference compounds at U and Am L_{III} edges obtained from the XANES spectra in figure 3. The standard uncertainty for E_0 and WL positions is ±0.2 eV, that for mole per cent is ±2 mol.%, that for O/M ratio is ±0.01. The value were measured at *RT* and at a pressure of (0.10 ± 0.01) MPa.

Sample	U L_{III}		Am L_{III}		Mole per cent (mol.%)					O/M
	E_0 /(eV)	WL/(eV)	E_0/(eV)	WL/(eV)	U^{+IV}	U^{+V}	U^{+VI}	Am^{+III}	Am^{+IV}	
$U_{0.90}Am_{0.10}O_{2\pm\delta}$	17169.9	17175.6	18512.5	18517.4	76	14	0	10	0	2.02
$U_{0.85}Am_{0.15}O_{2\pm\delta}$	17169.7	17175.6	18512.6	18517.4	71	14	0	15	0	2.00
$U_{0.80}Am_{0.20}O_{2\pm\delta}$	17170.8	17176.7	18512.4	18517.5	34	42	4	20	0	2.15
UO_2	17169.8	17175.4			100					
U_4O_9	17170.9	17176.3			50	50				
U_3O_8	17171.9	17179.5				67	33			
AmO_2			18514.0	18521.6				0	100	
Am^{+III}			18512.9	18517.7				100	0	

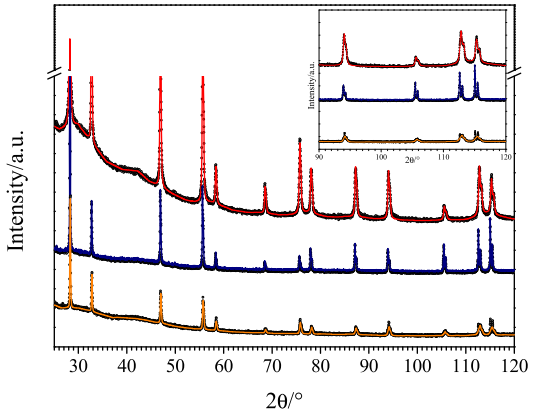

FIGURE 4. Experimental XRD patterns (scattered point) and respective fitting results (line) of laser-melted $U_{0.90}Am_{0.10}O_{2\pm\delta}$ (red), $U_{0.85}Am_{0.15}O_{2\pm\delta}$ (blue) and $U_{0.80}Am_{0.20}O_{2\pm\delta}$ (orange). (For interpretation of the references to colour in this figure legend, the reader is referred to the web version of this article.)

Debye–Waller factor is observed at the Am L_{III} edge. This might indicate that the interstitial O atoms are preferentially accommodated around the U atoms.

3.3.3. Structure of the $U_{0.80}Am_{0.20}O_{2\pm\delta}$ laser-melted samples

As shown in figure 4, the heat treatment led to the de-mixing of the $U_{0.80}Am_{0.20}O_{2\pm\delta}$ solid solution into two fluorite phases with close lattice parameters. Looking at figure 7, one can clearly see that the U L_{II} EXAFS spectrum of the $U_{0.80}Am_{0.20}O_{2\pm\delta}$ is different from that of UO_2 but close to that of U_4O_9. The U local environment is then similar to that of U in U_4O_9. This agrees actually with the U valence derived from XANES and the O/M of 2.15. The O/U is equal to 2.31, i.e. between U_4O_9 and U_3O_7. Considering that oxidation at room temperature from UO_2 to U_3O_7 occurs with an accumulation of cuboactohedron defects in the UO_2 fluorite structure, such a mechanism would imply that the U local environment between U_4O_9 and U_3O_7 would evolve only slightly. On the contrary, the Am L_{III} EXAFS spectrum of figure 7 indicates that Am remains in fluorite-type coordination. It is interesting to note that the U local environment is clearly modified while that of Am remains unchanged. This is in agreement with the increase of the Debye–Waller factors that has been observed solely around the U atoms for the $U_{0.90}Am_{0.10}O_{2\pm\delta}$ and $U_{0.85}Am_{0.15}O_{2\pm\delta}$ compounds. This difference of local environment clearly shows that U and Am are not randomly distributed in the cationic lattice contrary to $U_{0.90}Am_{0.10}O_{2\pm\delta}$ and $U_{0.85}Am_{0.15}O_{2\pm\delta}$. One can then assume that during the melting the solid solution de-mixed into a phase rich in Am with a UO_2 structure and into a phase poorer in Am with a U_4O_9 structure. It is however difficult to conclude on the cause of this de-mixing. One can actually imagine that the $U_{0.80}Am_{0.20}O_{2\pm\delta}$ solid solution de-mixes during the melting as the phase is not thermodynamically stable at high temperature. But one can also argue that the de-mixing occurred in this case, only because the as-synthesized $U_{0.80}Am_{0.20}O_{2\pm\delta}$ compound exhibited a lower cationic homogeneity compared to the initial $U_{0.90}Am_{0.10}O_{2\pm\delta}$ and $U_{0.85}Am_{0.15}O_{2\pm\delta}$ compounds. The formation, in $U_{0.80}Am_{0.20}O_{2\pm\delta}$, of an oxygen-richer phase can be linked to oxygen redistribution between the two phases. However, the occurrence of some unforeseen issues cannot be completely excluded, such as unwanted exposition of the sample to air traces during the experimental characterisation or uncontrolled leakage of the high-pressure vessel after the laser heating tests, leading to higher oxygen impurity content in the atmosphere in contact with the sample. This point will be clarified by further investigation, in particular by extending the analysis to compositions richer in americium.

It is also important to note that the UL_{II} EXAFS oscillations are well defined up to 110 nm^{-1} while the signal decreases significantly after 80 nm^{-1} for the Am L_{III}. This explains the decrease of the second TF peak corresponding to the Am-metal sphere. Therefore, the local environment around U is well defined despite the addition of O whereas a loss of order is observed after 4 Å around Am atoms.

4. Discussion

The melting/freezing point decrease reported in figure 2 for samples laser heated in pressurized argon is limited to less than $T = 100$ K for the maximum Am/(U + Am) content investigated here, 20 mol.%.

TABLE 4
Unit cell parameters of the laser-melted $U_{1-x}Am_xO_{2\pm\delta}$ and results of Rietveld refinement. The lattice parameter of the as-synthesized materials are also provided [5,40]. The data were measured at *RT* and at a pressure of (0.10 ± 0.01) MPa. The standard uncertainty of the lattice parameter is $\pm 5 \cdot 10^{-5}$ nm.

Sample	10 a/nm before melting	10 a/nm	10^3 V/nm^3	Space group	Rwp	Rp	GOF
$U_{0.90}Am_{0.10}O_{2\pm\delta}$	5.4680	5.4699	163.7	Fm-3 m (225)	2.69	1.95	1.72
$U_{0.85}Am_{0.15}O_{2\pm\delta}$	5.4641	5.4777	164.4	Fm-3 m (225)	4.84	3.25	1.58
$U_{0.80}Am_{0.20}O_{2\pm\delta}$	5.4611	5.4655	163.3	Fm-3 m (225)	3.89	2.62	1.38
		5.4729	163.9	Fm-3 m (225)			

$R_P = \Sigma[y_i(obs) - y_i(calc)]/\Sigma y_i(obs)$; $R_{wp} = \{\Sigma w_i\,[y_i(obs) - y_i(calc)]^2/\Sigma y_i(obs)\}^{1/2}$; GOF = R_{wp}/R_{exp}.

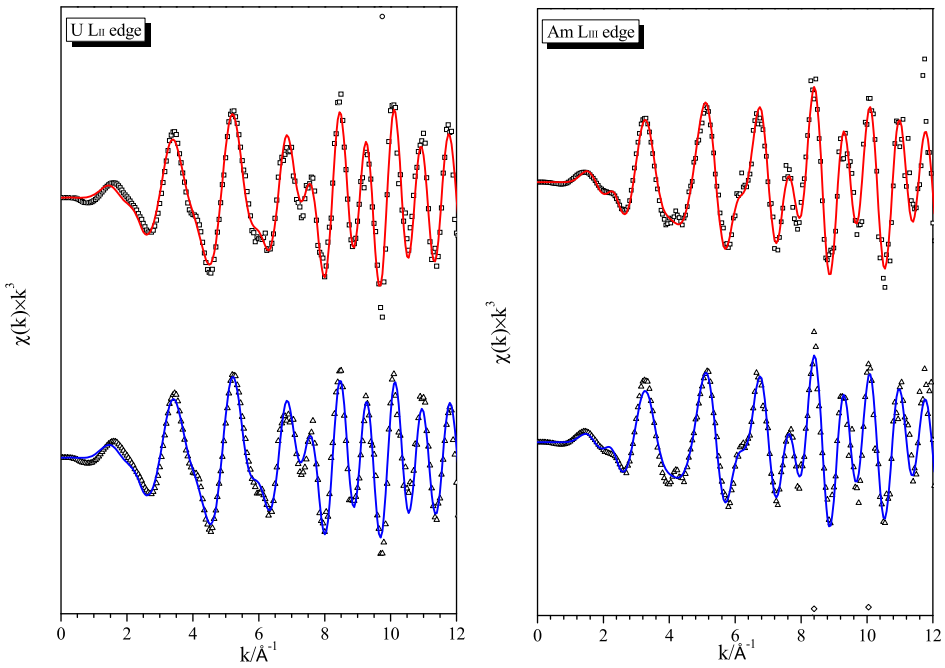

FIGURE 5. Experimental (scattered point) and fitted (line) k^3-weighted EXAFS spectra at U L_{II} (left) and Am L_{III} (right) of laser-melted $U_{0.90}Am_{0.10}O_{2\pm\delta}$ (red) and $U_{0.85}Am_{0.15}O_{2\pm\delta}$ (blue). Note that he label along the *x*-axis should read as 0.1 k/nm^{-1}. (For interpretation of the references to colour in this figure legend, the reader is referred to the web version of this article.)

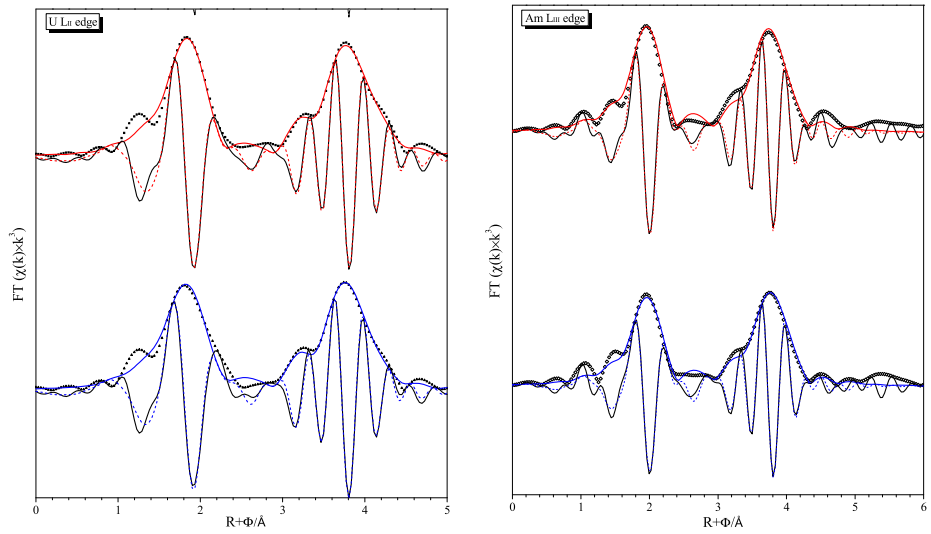

FIGURE 6. Experimental (scattered point) and fitted (line) Fourier transformed EXAFS spectra at U L_{II} (left) and Am L_{II} (right) of laser-melted $U_{0.90}Am_{0.10}O_{2\pm\delta}$ (red) and $U_{0.85}Am_{0.15}O_{2\pm\delta}$ (blue). The data are not phase corrected. The imaginary part of the Fourier transformed EXAFS spectra are presented. Note that he label along the *x*-axis should read as 0.1 k/nm^{-1}. (For interpretation of the references to colour in this figure legend, the reader is referred to the web version of this article.)

One can incidentally notice that the average melting/solidification (*solidus*) temperatures measured in the compositions $U_{0.90}Am_{0.10}O_{2\pm\delta}$ and $U_{0.85}Am_{0.15}O_{2\pm\delta}$ are very close (respectively T = (3070 ± 24) K and T = (3071 ± 29) K, whereas a clearer decrease is observed for $U_{0.8}Am_{0.2}O_{2+\delta}$. Of course based on these data one cannot exclude the occurrence, between $U_{0.90}Am_{0.10}O_{2\pm\delta}$ and $U_{0.85}Am_{0.15}O_{2\pm\delta}$, of a three-phase equilibrium boundary, possibly involving complex liquid/solid equilibria in the presence of a miscibility gap either in the liquid or in the solid. Such a phase boundary would then exist at a constant temperature, consistently with Gibbs' phase rule. This hypothesis, which would require more experimental data at intermediate compositions to be confirmed or ruled out, seems rather unlikely in (U, Am)$O_{2\pm\delta}$ compounds, at least by analogy with other better studied mixed actinide systems [23–27].

If one excludes the existence of such miscibility gaps, the similar average melting/solidification temperatures measured in the compositions $U_{0.90}Am_{0.10}O_{2\pm\delta}$ and $U_{0.85}Am_{0.15}O_{2\pm\delta}$ can be attributed to a simple statistical effect linked to the small size of the data sets. Then the current results would agree well with the ideal solution trend proposed by Kato et al. [27] for Am/(U + Am) contents up to 7 mol.%, plotted as a dotted line in figure 2, even though this model is a somewhat rough approximation. Besides the usual ideal solution approximation (i.e. zero mixing enthalpy), it actually

TABLE 5
Structural parameters obtained by fitting the EXAFS spectra at U L_{II} and Am L_{III} edges of the laser-melted $U_{1-x}Am_xO_{2\pm\delta}$ compounds presented in figures 5 and 6. The values were measured at *RT* and at a pressure of (0.10 ± 0.01) MPa. The standard uncertainties are provided in the table.

Sample	Edge	Sphere	10 Distance/nm	Coordination number	Debye–Waller factor: σ^2 (Å^2)	Correlation factor *R*
UO_2 (reference)	U L_{II}	O 1	2.355 ± 0.005	7.9 ± 0.5	0.0031 ± 0.0005	0.008 (domain: 1.6 to 6 Å)
		U 1	3.866 ± 0.005	11.9 ± 0.5	0.0015 ± 0.0005	
		O 2	4.52 ± 0.01	26 ± 2	0.005 ± 0.002	
		U 2	5.46 ± 0.02	6 ± 0.5	0.003 ± 0.001	
$U_{0.90}Am_{0.10}O_{2\pm\delta}$	U L_{II}	O 1	2.334 ± 0.005	8.2 ± 0.5	0.009 ± 0.001	0.011 (domain: 1.6 to 5 Å)
		Am/U 1	3.87 ± 0.01	12.1 ± 0.5	0.007 ± 0.001	
		O 2	4.52 ± 0.01	26 ± 2	0.008 ± 0.002	
	Am L_{III}	O 1	2.420 ± 0.005	8.1 ± 0.5	0.007 ± 0.001	0.023 (domain: 1.6 to 5 Å)
		Am/U 1	3.86 ± 0.01	11.9 ± 0.5	0.006 ± 0.001	
		O 2	4.49 ± 0.02	23 ± 2	0.015 ± 0.002	
$U_{0.85}Am_{0.15}O_{2\pm\delta}$	U L_{II}	O 1	2.329 ± 0.005	8.0 ± 0.5	0.010 ± 0.001	0.014 (domain: 1.6 to 5 Å)
		Am/U 1	3.86 ± 0.01	12.2 ± 0.5	0.007 ± 0.001	
		O 2	4.54 ± 0.01	23 ± 2	0.011 ± 0.002	
	Am L_{III}	O 1	2.433 ± 0.005	7.8 ± 0.5	0.008 ± 0.001	0.013 (domain: 1.6 to 5 Å)
		Am/U 1	3.87 ± 0.01	11.8 ± 0.5	0.007 ± 0.001	
		O 2	4.51 ± 0.02	25 ± 2	0.015 ± 0.002	

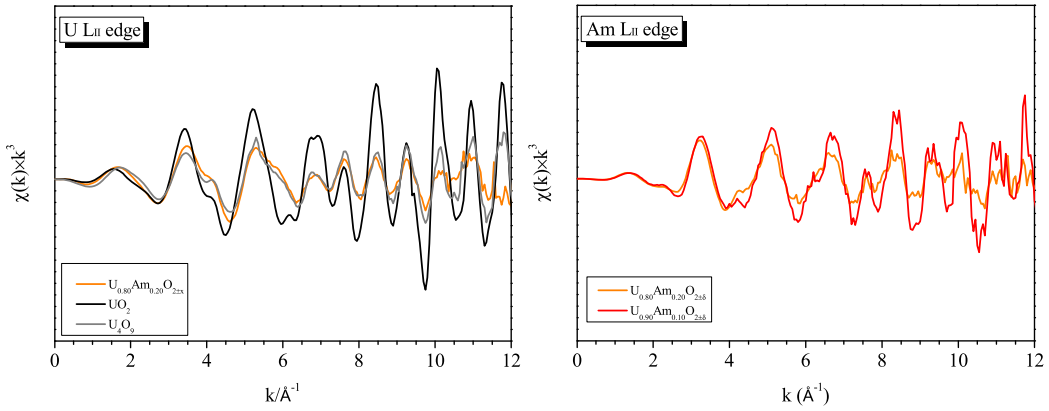

FIGURE 7. Experimental k^3-weighted EXAFS spectra at U L_{II} (left) and Am L_{II} (right) of laser-melted $U_{0.80}Am_{x.20}O_{2\pm\delta}$ (orange) and respective references. Note that he label along the *x*-axis should read as 0.1 *k*/nm^{-1}. (For interpretation of the references to colour in this figure legend, the reader is referred to the web version of this article.)

assumes equal heat capacities for both UO_2 and AmO_2, and it relies on a fictitious melting point of AmO_2 extrapolated to T = 2773 K by Kato et al. [27]. Nonetheless, it can be deduced from the present results that a similar ideal solution behaviour is most likely followed by the (U, Am)O_2 mixture at temperatures close to melting to an even larger extent than assumed by Kato et al. Apparently, this ideal solution behaviour seems even to be compatible with a complete reduction of Am to Am^{+III}, at least for the current low Am-doping levels. Such a behaviour is approximately followed at lower temperatures by similar solid state solutions between UO_2 and trivalent cation oxides such as Bi_2O_3 and La_2O_3 [48,49]. In reality, the fact that high-temperature ideal solution behaviour is observed brings along no certainty about the system behaviour at lower temperatures, where the cation valence states were measured by XAS analysis. In fact, thermal excitation can cure crystal defects and asymmetries that would result in strongly non-ideal behaviour at temperatures closer to the ambient one, as already observed, for example, in systems like (UO_2 + ZrO_2) [50]. Only by measuring the cation valence temperature dependence and by consistently modelling the corresponding phase equilibria it would be possible to exhaustively describe the (UO_2 + AmO_2) system from room to melting temperature. Because of the very likely changes in the oxygen content linked with the valence change and, at higher temperatures, with non-congruent vapourization, such phase boundary modelling should be extended to the whole (U + Am + O) ternary system, and cannot be limited to the (UO_2 + AmO_2) pseudo-binary plane.

Another point worth discussion is the effect of self-irradiation on the phase stability in the (UO_2 + AmO_2) system. First, even though the samples were not free of self-irradiation-induced damage before the laser heating experiments, radiation damage is cured at temperatures exceeding 2000 K [51], so even more efficiently in the current experimental conditions. However, because a delay of few weeks (for XRD) to a couple of months (for XAS) was inevitable between the laser heating/cooling treatments and the post-melting material characterisation, the samples underwent some self-irradiation damage, notably those with the highest Am content. This could be viewed as a partial explanation for the complex phase splitting and higher O/M ratio observed in the $U_{0.8}Am_{0.2}O_{2+\delta}$ sample as several studies have shown that α-self-irradiation-induced structural effects on (U, Am)O_2 compounds are limited to lattice swelling reaching up to 0.8 vol.% and a small structural disorder increase [45,46,52–54].

In conclusion, the main message of this work is that the melting temperature of Am-doped UO_2 decreases to a limited extent (not more than T = 80 to 90 K) and follows an approximately ideal solution behaviour up to an Am/(U + Am) content of 20 mol.%. This is utterly true provided the experimental conditions under which melting is obtained are such as to maintain, at high temperature, an approximate oxygen stoichiometry (i.e. O/M = 2.00) without

phase separation. A more comprehensive knowledge of the (U + Am + O) thermodynamic system is required to prove up to which extent, these conditions were met under the inert atmosphere used in this study (pressurized argon).

5. Conclusion

The melting behaviour of (uranium + americium) dioxide mixed with Am/(U + Am) ratios up to 20 mol.% has been experimentally studied. Although a vast amount of further research is still needed for an exhaustive definition of phase boundaries in the (U + Am + O) system, sound conclusions can already be drawn from the present, first investigation. The average solid/liquid transition temperatures are (3070 ± 24) K, (3071 ± 29) K and (3051 ± 28) K, for Am/(U + Am) ratios of 10, 15 and 20 mol.%. In this case, the melting/solidification point decreases from $T = 3120$ K in pure UO_2 to $T = 3051$ K in $U_{0.8}Am_{0.2}O_{2\pm\delta}$, following a trend similar to that of an ideal solution assuming, in line existing literature, an extrapolated melting point of AmO_2 around $T = 2773$ K. This would also mean that if the compositions studied here are laser-heated under an inert atmosphere, their oxygen-to-metal ratios remain close to the initial 2.00 value. This high-temperature ideal solution behaviour is evidently compatible with the coexistence – proven by pre-and post-melting XANES analysis, of U^{+IV} U^{+V} and Am^{+III}. However, no clear indication about the validity of such ideal solution behaviour at lower temperatures can be inferred based on the current results.

Acknowledgement

The authors acknowledge the European Synchrotron Radiation Facility and the FP7 Talisman project for provision of synchrotron radiation facilities at the Rossendorf Beamline. The authors are indebted to M. Bataille, P. Coste, S. Gardeur, H. Hein and P. Lajarge for their help during the sample synthesis. M. Caisso and F. Lebreton thank the CEA PACFA program for financial support through Ph. D. funding.

References

[1] M. Salvatores, G. Palmiotti, Prog. Part. Nucl. Phys. 66 (2011) 144–166, http://dx.doi.org/10.1016/j.ppnp.2010.10.001.
[2] D. Westlén, Prog. Nucl. Energy 49 (2007) 597–605, http://dx.doi.org/10.1016/j.pnucene.2007.02.002.
[3] C. Chabert, D. Warin, J.-F. Milot, A. Saturnin, A. Leudet, M.H. Lagrange, et al., Impact of minor actinide transmutation options on interim storage and geological disposal: the French Case, in: OECD-NEA, Prague, République Tchèque, 2012.
[4] D. Prieur, A. Jankowiah, T. Delahaye, N. Herlet, P. Dehaudt, P. Blanchart, J. Nucl. Mater. 414 (2011) 503–507, http://dx.doi.org/10.1016/j.jnucmat.2011.05.036.
[5] M. Vespa, M. Rini, J. Spino, T. Vitova, J. Somers, J. Nucl. Mater. 421 (2012) 80–88, http://dx.doi.org/10.1016/j.jnucmat.2011.11.055.
[6] F. Lebreton, R.C. Belin, D. Prieur, T. Delahaye, P. Blanchart, Inorg. Chem. 51 (2012) 9369–9375, http://dx.doi.org/10.1021/ic301124d.
[7] T. Delahaye, F. Lebreton, D. Horlait, N. Herlet, P. Dehaudt, J. Nucl. Mater. 432 (2013) 305–312, http://dx.doi.org/10.1016/j.jnucmat.2012.07.018.
[8] F. Lebreton, D. Horlait, T. Delahaye, P. Blanchart, J. Nucl. Mater. 439 (2013) 99–102, http://dx.doi.org/10.1016/j.jnucmat.2013.03.074.
[9] D. Horlait, F. Lebreton, A. Gauthé, M. Caisso, B. Arab-Chapelet, S. Picart, et al., J. Nucl. Mater. 444 (2014) 181–185, http://dx.doi.org/10.1016/j.jnucmat.2013.09.028.
[10] E. Remy, S. Picart, T. Delahaye, I. Jobelin, F. Lebreton, D. Horlait, et al., J. Nucl. Mater. 453 (2014) 214–219, http://dx.doi.org/10.1016/j.jnucmat.2014.06.048.
[11] M. Caisso, S. Picart, R.C. Belin, F. Lebreton, P.M. Martin, K. Dardenne, et al., Dalton Trans. 44 (2015) 6391–6399, http://dx.doi.org/10.1039/C4DT03515A.
[12] S. Bejaoui, Americium-Bearing Blanket Separate-effect Experiments: MARIOS and DIAMINO Irradiations, in: Proc. Glob. 2011, Makuhari, Japan, 2011.
[13] E. D'Agata, P.R. Hania, S. Bejaoui, C. Sciolla, T. Wyatt, M.H.C. Hannink, et al., Ann. Nucl. Energy. 62 (2013) 40–49, http://dx.doi.org/10.1016/j.anucene.2013.05.043.
[14] W. Bartscher, C. Sari, J. Nucl. Mater. 118 (1983) 220–223, http://dx.doi.org/10.1016/0022-3115(83)90228-3.
[15] K. Mayer, B. Kanellakopoulos, J. Naegele, L. Koch, J. Alloys Compd. 213–214 (1994) 456–459, http://dx.doi.org/10.1016/0925-8388(94)90960-1.
[16] T. Nishi, M. Nakada, C. Suzuki, H. Shibata, Y. Okamoto, M. Akabori, et al., J. Nucl. Mater. 418 (2011) 311–312, http://dx.doi.org/10.1016/j.jnucmat.2011.07.016.
[17] D. Prieur, P.M. Martin, A. Jankowiak, E. Gavilan, A.C. Scheinost, N. Herlet, et al., Inorg. Chem. 50 (2011) 12437–12445, http://dx.doi.org/10.1021/ic200910f.
[18] D. Prieur, P. Martin, F. Lebreton, T. Delahaye, D. Banerjee, A.C. Scheinost, et al., J. Nucl. Mater. 434 (2013) 7–16, http://dx.doi.org/10.1016/j.jnucmat.2012.11.037.
[19] O.S. Vălu, D. Staicu, O. Beneš, R.J.M. Konings, P. Lajarge, J. Alloys Compd. 614 (2014) 144–150, http://dx.doi.org/10.1016/j.jallcom.2014.05.083.
[20] D. Prieur, F. Lebreton, P. Martin, M. Caisso, R. Butzbach, A.C. Scheinost, et al., J. Solid State Chem. 230 (2015) 8–13, http://dx.doi.org/10.1016/j.jssc.2015.03.037.
[21] D. Manara, C. Ronchi, M. Sheindlin, M. Lewis, M. Brykin, J. Nucl. Mater. 342 (2005) 148–163, http://dx.doi.org/10.1016/j.jnucmat.2005.04.002.
[22] F. De Bruycker, K. Boboridis, D. Manara, P. Pöml, M. Rini, R.J.M. Konings, Mater. Today 13 (2010) 52–55, http://dx.doi.org/10.1016/S1369-7021(10)70204-2.
[23] F. De Bruycker, K. Boboridis, P. Pöml, R. Eloirdi, R.J.M. Konings, D. Manara, J. Nucl. Mater. 416 (2011) 166–172, http://dx.doi.org/10.1016/j.jnucmat.2010.11.030.
[24] F. De Bruycker, K. Boboridis, R.J.M. Konings, M. Rini, R. Eloirdi, C. Guéneau, et al., J. Nucl. Mater. 419 (2011) 186–193, http://dx.doi.org/10.1016/j.jnucmat.2011.08.028.
[25] R. Böhler, M.J. Welland, D. Prieur, P. Cakir, T. Vitova, T. Pruessmann, et al., J. Nucl. Mater. 448 (2014) 330–339, http://dx.doi.org/10.1016/j.jnucmat.2014.02.029.
[26] D. Prieur, R.C. Belin, D. Manara, D. Staicu, J.-C. Richaud, J.-F. Vigier, et al., J. Alloys Compd. 637 (2015) 326–331, http://dx.doi.org/10.1016/j.jallcom.2015.03.032.
[27] M. Kato, K. Morimoto, H. Sugata, K. Konashi, M. Kashimura, T. Abe, J. Nucl. Mater. 373 (2008) 237–245, http://dx.doi.org/10.1016/j.jnucmat.2007.06.002.
[28] K. Richter, A. Fernandez, J. Somers, J. Nucl. Mater. 249 (1997) 121–127, http://dx.doi.org/10.1016/S0022-3115(97)00232-8.
[29] M. Kato, K. Morimoto, H. Sugata, K. Konashi, M. Kashimura, T. Abe, J. Alloys Compd. 452 (2008) 48–53, http://dx.doi.org/10.1016/j.jallcom.2007.01.183.
[30] V. Petříček, M. Dušek, L. Palatinus, Z. Für Krist. – Cryst. Mater. 229 (2014), http://dx.doi.org/10.1515/zkri-2014-1737.
[31] W. Matz, N. Schell, G. Bernhard, F. Prokert, T. Reich, J. Claußner, et al., J. Synchrotron Radiat. 6 (1999) 1076–1085, http://dx.doi.org/10.1107/S0909049599010663.
[32] M. Newville, J. Synchrotron Radiat. 8 (2001) 322–324, http://dx.doi.org/10.1107/S0909049500016964.
[33] B. Ravel, M. Newville, J. Synchrotron Radiat. 12 (2005) 537–541, http://dx.doi.org/10.1107/S0909049505012719.
[34] L. Desgranges, G. Baldinozzi, D. Siméone, H.E. Fischer, Inorg. Chem. 50 (2011) 6146–6151, http://dx.doi.org/10.1021/ic200316b.
[35] K.O. Kvashnina, S.M. Butorin, P. Martin, P. Glatzel, Phys. Rev. Lett. 111 (2013) 253002, http://dx.doi.org/10.1103/PhysRevLett. 111.253002.
[36] B. Arab-Chapelet, S. Grandjean, G. Nowogrocki, F. Abraham, J. Alloys Compd. 444–445 (2007) 387–390, http://dx.doi.org/10.1016/j.jallcom.2007.01.033.
[37] B. Arab-Chapelet, S. Grandjean, G. Nowogrocki, F. Abraham, J. Nucl. Mater. 373 (2008) 259–268, http://dx.doi.org/10.1016/j.jnucmat.2007.06.004.
[38] P. Martin, S. Grandjean, C. Valot, G. Carlot, M. Ripert, P. Blanc, et al., J. Alloys Compd. 444–445 (2007) 410–414, http://dx.doi.org/10.1016/j.jallcom.2007.01.032.
[39] U. Carvajal-Nunez, D. Prieur, T. Vitova, J. Somers, Inorg. Chem. 51 (2012) 11762–11768, http://dx.doi.org/10.1021/ic301709d.
[40] D. Prieur, U. Carvajal-Nunez, T. Vitova, J. Somers, Eur. J. Inorg. Chem. 2013 (2013) 1518–1524, http://dx.doi.org/10.1002/ejic.201201294.
[41] D. Prieur, F. Lebreton, P.M. Martin, M. Caisso, R. Butzbach, J. Somers, et al., J. Solid State Chem. 230 (2015) 8–13, http://dx.doi.org/10.1016/j.jssc.2015.03.037.
[42] D. Prieur, F. Lebreton, P.M. Martin, A. Jankowiak, T. Delahaye, P. Dehaudt, et al., J. Eur. Ceram. Soc. 32 (2012) 1585–1591, http://dx.doi.org/10.1016/j.jeurceramsoc.2011.12.017.
[43] T. Nishi, M. Nakada, C. Suzuki, H. Shibata, A. Itoh, M. Akabori, et al., J. Nucl. Mater. 401 (2010) 138–142, http://dx.doi.org/10.1016/j.jnucmat.2010.04.011.
[44] R.D. Shannon, Acta Crystallogr. Sect. A 32 (1976) 751–767, http://dx.doi.org/10.1107/S0567739476001551.
[45] D. Prieur, P.M. Martin, F. Lebreton, T. Delahaye, A. Jankowiak, J.-P. Laval, et al., J. Solid State Chem. 194 (2012) 206–211, http://dx.doi.org/10.1016/j.jssc.2012.05.006.
[46] F. Lebreton, P.M. Martin, D. Horlait, R. Bès, A.C. Scheinost, A. Rossberg, et al., Inorg. Chem. 53 (2014) 9531–9540, http://dx.doi.org/10.1021/ic500681k.
[47] F. Lebreton, D. Horlait, R. Caraballo, P.M. Martin, A.C. Scheinost, A. Rossberg, et al., Inorg. Chem. (2015), http://dx.doi.org/10.1021/acs.inorgchem.5b01357.
[48] K. Popa, O. Beneš, P.E. Raison, J.C. Griveau, P. Pöml, E. Colineau, R.J.M. Konings, J. Somers, J. Nucl. Mater. 465 (2015) 653–656, http://dx.doi.org/10.1016/j.jnucmat.2015.06.055.
[49] Z. Talip, T. Wiss, P.E. Raison, J. Paillier, D. Manara, J. Somers, R.J.M. Konings, J. Am. Ceram. Soc. 98 (2015) 2278–2285, http://dx.doi.org/10.1111/jace.13559.

[50] P. Piluso, G. Trillon, C. Journeau, J. Nucl. Mater. 344 (2005) (2000) 259–264, http://dx.doi.org/10.1016/j.jnucmat.2005.04.052.
[51] D. Prieur, G. Pagliosa, J. Spino, R. Caciuffo, J. Somers, R. Eloirdi, J. Solid State Chem. 199 (2013) 334–337, http://dx.doi.org/10.1016/j.jssc.2012.12.022.
[52] D. Prieur, A. Jankowiak, D. Roudil, S. Dubois, C. Leorier, N. Herlet, et al., J. Nucl. Mater. 411 (2011) 15–19, http://dx.doi.org/10.1016/j.jnucmat.2010.12.314.
[53] D. Horlait, F. Lebreton, P. Roussel, T. Delahaye, Inorg. Chem. 52 (2013) 14196–14204, http://dx.doi.org/10.1021/ic402124s.
[54] D. Prieur, J.-F. Vigier, T. Wiss, A. Janssen, J. Rothe, A. Cambriani, et al., J. Solid State Chem. 212 (2014) 7–12, http://dx.doi.org/10.1016/j.jssc.2013.12.016.

JCT 15-768